Two- And Three-Photon Resonances in Rydberg Atoms for Localized Measurement

A thesis submitted in partial fulfillment of the requirement
for the degree of Bachelor of Science with Honors in
Physics from the College of William and Mary in Virginia,

by

Kevin Su

Accepted for Honors

_____

Advisor: Prof. Irina Novikova

_____

Prof. Saskia Mordijck

_____

Prof. Gunter Luepke

Williamsburg, Virginia
April 28 2025

Contents

Acknowledgments

Thank you to Prof. Novikova for guidance throughout this thesis project and my undergraduate experience. Thank you to Rob Behary for being my direct mentor in the lab. Thank you to the whole AMO group at W&M, especially Nic and Ziqi for always being in the lab to help with coding and technical problems. Thank you to Prof. Mikhailov and Prof. Aubin for their help and comments. Thank you to Prof. Mordjick and Prof. Luepke for serving on my thesis committee. Thank you to my family and friends for their support throughout college.

List of Figures

Abstract

In this project, we investigated methods to make localized measurement of electric field with Rydberg electromagnetically induced transparency (EIT). Under EIT, opaque medium becomes transparent to near resonance optical fields. It is usually implemented with two laser beams completely overlapped, which can probe atomic response to external electric field precisely but lack spatial resolution. We proposed three different methods to obtain spatial information about electric field distribution. First we studied the modifications of Rydberg EIT resonances in non-collinear geometry, when two laser fields cross at a non-zero angle. We compared resonances in crossed-beam with collinear geometry and observed strong broadening and weakening of EIT resonance even when crossing angle is small. Our results show the tradeoff between spectroscopic sensitivity and spatial resolution of crossed-beam EIT. We also explored fluorescence imaging as an alternative way of making spatially resolved measurement. Lastly, we observed Rydberg EIT resonance in three-photon excitation scheme and reported our progress toward implementing three-photon EIT to perform localized, Doppler-free measurement.

Chapter 1

Introduction

Electric field measurement has a wide range of applications, because it allows, for example, diagnostics of various parameters of charged objects. Most electrometers today require having a physical probe at the region of interests to do the measurement. This design is invasive as the presence of a probe changes the electric environment while making measurement. As shown in Fig.1.1, examples of this type of electrometer include Langmuir probe, which is used to measure electric potential inside plasma, and "harp-scanner", which is used to track charged particle beams in accelerators.

A potential way to do non-invasive electrometry is using atoms. When atoms are in the highly excited Rydberg state, they become sensitive to external electromagnetic environment. Their response can be probed using optical methods, and thus being non-invasive. This property makes them candidates to measure electric field. Many research groups have demonstrated using Rydberg atoms to build detectors for dc and rf-electric fields [1, 2, 3]. Many of these applications involve a process known as electromagnetically induced transparency (EIT). EIT is usually achieved by shining two laser fields tuned at the right frequencies to the atoms. The narrow spectral width of the EIT resonance allows people to probe the response of Rydberg atoms to electric fields with high precision. However, in practical settings, atoms are usually put in room-temperature vapor cells, and thermal motion of atoms leads to Doppler
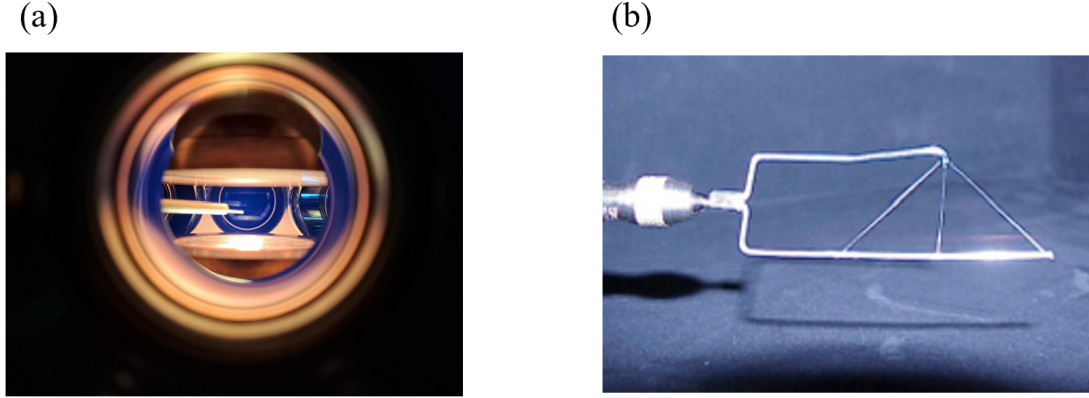
Figure 1.1: Picture of (a) Langmuir probe that is used to measure electric potential of plasma by inserting an electrode inside and (b) "harp-scanner" to detect electron beam in accelerator.

broadening of the EIT resonance, which limits the sensitivity.

To minimize Doppler broadening, people usually set two lasers to be parallel, propagating in opposite direction, and spatially overlapped throughout the vapor cell, as shown in Fig.1.2(a). One drawback of this geometry is that it integrates the signal along the beam path, and thus it cannot make localized measurement. If an electric field is spatially non-uniform, such as the field inside plasma, EIT in collinear geometry cannot probe the spatial variation.

In order to do localized sensing with Rydberg EIT, three potential solutions are investigated. The first one is to cross two laser beams at an angle like in Fig.1.2(b) so that only the electric field within crossing region of the beams is measured. However, this non-collinear geometry will decrease the spectral resolution of EIT resonance due to additional Doppler broadening. To avoid the loss of spectral sensitivity, we tried to observe EIT resonance via fluorescence imaging, which enables localized measurement with collinear beam geometry. Finally, we explored three-photon EIT that could improve sensitivity further when three laser beams are crossed in star-like geometry to achieve Doppler-free excitiation.
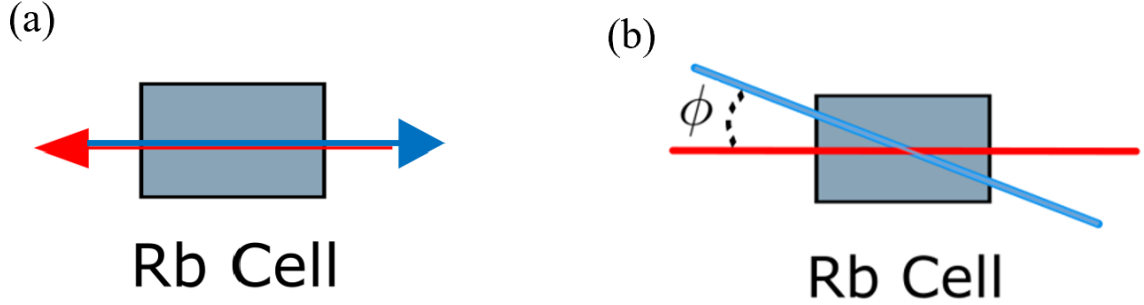
Figure 1.2: Collinear (a) and non-collinear (b) geometry of two laser beams.

This thesis is structured as follows. In Chapter 2, we give a theory overview of Rydberg EIT and Doppler broadening of EIT in hot atomic vapor. In Chapter 3, we present our experiment and discuss observed transmission spectra in non-collinear geometry. We compare our experimental data with our numerical model results and show the impact of transverse velocity on the spectra. In Chapter 4, we discuss fluorescence imaging as another way of observing EIT resonances, and we show it is able to do localized measurement with collinear beams and confirm our results on Doppler broadening of EIT resonances. Chapter 5 focuses on our progress toward using three-photon EIT to do localized measurement, which can be Doppler-free with star-like beam geometry.

Chapter 2

Theory Overview

This chapter gives an overview of theory background of our project. Two major topics are included: Electromagnetically induced transparency (EIT) in ladder scheme and Doppler effect on EIT resonance in hot atomic vapor due to wavelength mismatch.

2.1   Ladder Scheme Rydberg EIT

EIT can make opaque medium to be transparent to near resonance optical fields. In a typical two-photon EIT setup, a medium such as a gas of atoms is illuminated by a weak probe field and a strong coupling field, as shwon in Fig.2.1(a). When only the probe field is present, the atoms absorb some of the light with frequency near resonance, as shown on the transmission Fig.2.1(b). The second optical field is added to connect the excited state with another long-lived atomic state. When two fields are at exact two-photon resonance, atoms do not absorb photons from the fields. This leads to an increase in transmission of the probe laser, and as a result, a peak appears at the bottom of the spectrum, as shown in Fig.2.1(c).

The most intuitive explanation of EIT involves a concept of "dark" state, in which an atom does not interact with either of the laser fields. First consider a simple three-level system shown in Fig.2.1(a). $|g\rangle$ is the ground state, $|e\rangle$ is the excited state, and $|r\rangle$ is the highly excited Rydberg state. The probe field couples to the transition
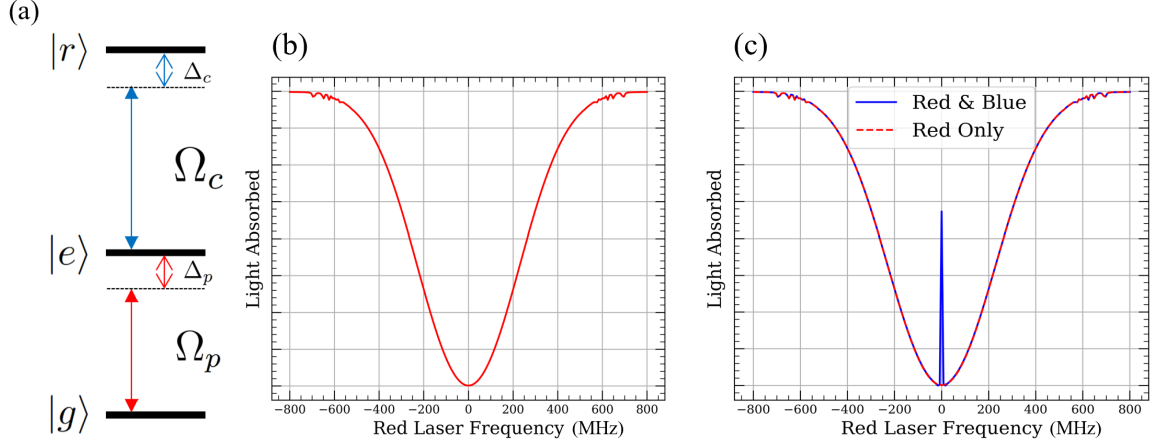
Figure 2.1: (a) Energy level diagram of general ladder scheme two-photon EIT. (b) Transmission spectrum of probe field with only the probe field illuminating the atoms. (c) Same as (b) but with near resonance coupling field illuminating atoms at the same.

$|g\rangle \rightarrow |e\rangle$ with Rabi frequency Ω_p, which indicates the strength of the coupling. The coupling field connects the transition from $|e\rangle \rightarrow |r\rangle$ with Rabi frequency Ω_c. Detunings $\Delta_p = \omega_{ge} - \omega_p$ and $\Delta_c = \omega_{er} - \omega_c$ are the frequency difference between probe and coupling fields and energy splittings of their corresponding transitions.

The Hamiltonian of the three-level system with two optical fields near resonance in rotating frame can be written as:

$$\hat{H} = \frac{\hbar}{2} \begin{pmatrix} 0 & \Omega_p^* & 0 \\ \Omega_p & -2\Delta_p & \Omega_c^* \\ 0 & \Omega_c & -2\delta \end{pmatrix} \tag{2.1}$$

where $\delta = \Delta_p + \Delta_c$ is the two-photon detuning [4].

One property of this Hamiltonian is the existence of eigenstate with eigenvalue of zero when two-photon detuning $\delta = 0$. This eigenstate is called the dark state because it is decoupled from both fields. Expression of the dark state is
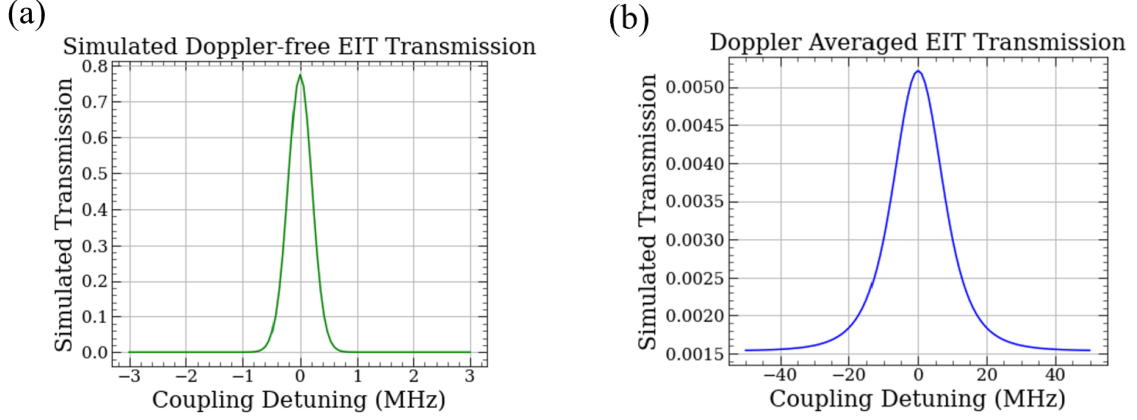
Figure 2.2: (a) Simulated Doppler-free transmission spectra of probe laser with probe laser on-resonance and coupling laser scanned across transition. (b) Same as (a) but is Doppler averaged over velocity distribution in hot atomic vapor.

$$|D\rangle = \frac{1}{\sqrt{|\Omega_p|^2 + |\Omega_c|^2}}(\Omega_p |r\rangle - \Omega_c |g\rangle) \tag{2.2}$$

Notice that the dark state is only a superposition of state $|g\rangle$ and $|r\rangle$, and population of each state only depends upon the Rabi frequencies. Therefore, to let majority of atoms being in the ground state, a weak probe field and strong coupling field setting is usually used in experiments.

When probe laser is locked on resonance ($\Delta_p = 0$) and coupling laser is scanned across transition, intensity of probe laser transmitted through the atoms can be plotted as a function of coupling detuning Δ_c as in Fig.2.2(a). Because atoms are in dark state if $\delta = \Delta_p + \Delta_c = 0$, a peak shows up at $\Delta_c = 0$.

Sensing of electric field can be done by monitoring the spectral shift or splitting of the peak [2, 3]. When exposed to an external electric field, Rydberg sublevels are shifted by:

$$h \cdot \Delta f_{|m_j|}(E) \approx -\frac{1}{2}\alpha_{|m_j|}E^2. \tag{2.3}$$

6
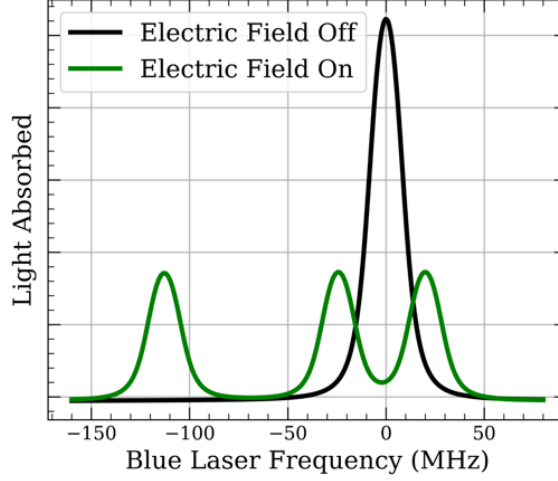
Figure 2.3: Simulated spectrum of EIT resonances with and without external electric field.

where h is Planck's constant, $\alpha_{|m_j|}$ is the scalar polarizability of the different $|m_j|$ sublevels of the Rydberg state and E is the magnitude of the electric field [5]. As a result, the EIT peak is split into several sub-peaks that each corresponds to a sublevel. Fig.2.3 shows the simulated splitting of the EIT peak when an external electric field is present. The splitting of the sub-peaks depends on the strength of electric field, which is the main mechanism to make the measurement. As a result, width of the EIT peak without presence of electric field is related to the sensitivity can be achieved. Ideally, the linewidth can be narrow as hundreds of kHz for stationary atoms, but it is much broader for atomic vapor. One factor that leads to broadening is the Doppler effect, which is discussed in the next section.

2.2 Doppler Effect in Atomic Vapor

Doppler effect is the change in frequency of wave due to the relative motion of observer and source of the wave. Unlike cold atom systems where atoms are nearly stationary, atoms in a room-temperature vapor cell have average velocity of few hundreds m/s

and velocity distribution following Maxwell-Boltzmann distribution. As a result, we need to consider that atoms in vapor cell with different velocities see the laser field at different frequencies.

The previous section shows that EIT happens when two-photon resonance condition $\delta = 0$ is satisfied. It is defined as $\delta = \Delta_p + \Delta_c$ in ideal scenario, but a velocity-dependent term is added to the equation to account for thermal velocity of atoms. In this case, two-photon detuning can be rewritten as

$$\delta(\vec{v}) = \delta_0 - (\vec{k}_p + \vec{k}_c) \cdot \vec{v} \tag{2.4}$$

where δ_0 is two-photon detuning for stationary atom, $\vec{k}_p = \frac{2\pi}{\lambda_p}$ and $\vec{k}_c = \frac{2\pi}{\lambda_c}$ are the wave vectors of probe and coupling field respectively, and $\vec{v}$ is the velocity of atom [2]. This velocity-dependent term indicates that atoms with different thermal velocities are on resonance with different coupling laser detunings, which broadens EIT peak. The narrowest linewidth is achieved when this term is minimized.

It is obvious that the velocity dependent term is minimum when $\vec{k}_p$ and $\vec{k}_c$ are in opposite directions, which is why probe and coupling laser are usually arranged to be counter-propagating in experiments. Hence, highest and narrowest EIT resonance is expected when probe and coupling beams counter-propagate.

Additionally, note that in our case of Rydberg EIT with ^{85}Rb, probe laser wavelength $\lambda_p \approx 780$nm and coupling laser wavelength $\lambda_c \approx 480$nm are used. The wavelength mismatch between probe and coupling field dictates that it is impossible to completely cancel out the velocity-dependent term. Therefore, even in counter-propagating geometry, EIT peak is still much wider than that in Doppler-free condition, as shown in Fig.2.2. The next chapter will discuss quantitatively how the Doppler broadening affects EIT resonance if it is implemented in non-collinear geometry.

Chapter 3

Rydberg EIT Spectra in Non-collinear Geometry

This chapter discusses our experiment of Rydberg EIT spectroscopy through [85]Rb atomic vapor with probe and coupling beam crossed at an non-zero angle for localized measurement. Our results show strong broadening and amplitude reduction of EIT resonance even when crossing angle is small.

3.1   Experimental Setup and Methods

Rydberg EIT is implemented in a [85]Rb vapor cell using two laser beams in the experiment. Fig.3.1(a) shows a simplified energy diagram of the system. The infrared probe laser ($\lambda_p \simeq 780$ nm) is tuned and locked to the bottom of the $5S_{1/2}$ $F = 3 \to 5P_{3/2}$ F' optical transition using absorption spectroscopy implemented in a Rb reference cell. The probe beam is roughly collimated to diameter of 0.6 mm, and its transmission through a Rb vapor cell is monitored to detect the EIT resonances. A cylindrical glass cell (diameter 2 cm, length 2.5 cm) heated to 37°C is used in experiment. The coupling laser ($\lambda_c \simeq 480$ nm, beam diameter 0.6 mm) is scanned across transition from $5P_{3/2}$ to Rydberg states $45D_{3/2}$ and $45D_{5/2}$. Power of the probe laser beam is kept low to approximately $P_p \simeq 75$ μW before going through the vapor cell, and power
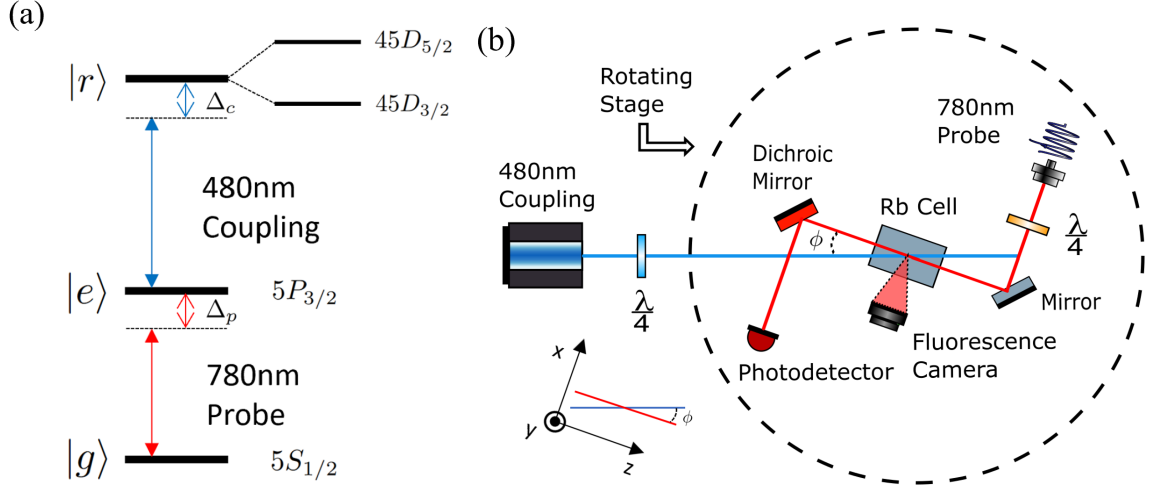
Figure 3.1: (a) Energy level diagram of ^{85}Rb. (b) Experimental setup schematic. $\frac{\lambda}{4}$: quarter waveplate. ϕ: crossing angle between two laser beams. $\phi = 0°$ is counter-propagation.

of the coupling beam is $P_c \simeq 35$mW before going through the cell. The weak probe, strong coupling setting is to let most of the population to be in the ground state as suggested by Eq.2.1. And both probe and coupling laser are set to be circularly polarized by quarter waveplate to maximize the $45D_{5/2}$ resonance [1].

A schematic of the experimental setup is presented in Fig.3.1(b). In order to control the angle between the probe and coupling beam, the fiber output of probe laser, Rb vapor cell, and the amplified photodetector used to measure the output probe field power are mounted on a rotational platform. Their relative positions are unchanged during experiments. The coupling laser is stationary on the optics table. The cell is placed at the center of the platform such that rotating the platform always keeps the intersection point of two laser beams to be in the center of the cell. For convenience, the coordinate is defined to be on the rotating platform so that only the coupling beam moves in that coordinate. Angle ϕ is the crossing angle between probe and coupling laser beam. Note that $\phi = 0°$ when probe and coupling beams
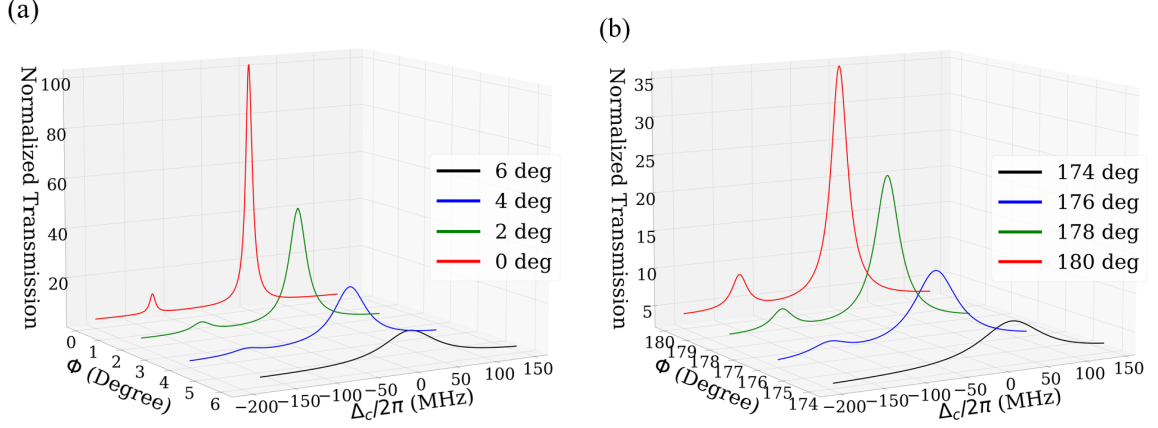
Figure 3.2: (a) Traces of EIT resonances recorded with nearly counter-propagating probe and coupling fields, crossing at a small angle $\phi \approx 0$. Taller peak corresponds to transition to $45D_{5/2}$ state and smaller peak to $45D_{3/2}$. (b) Same as (a) but for nearly co-propagating laser beams ($\phi \approx 180°$). For all transmission spectra, the zero coupling laser detuning is set to zero at the top of the $45D_{5/2}$ EIT resonance, and transmission is normalized to the highest peak observed at zero detuning and $\phi = 0$.

counter-propagating, since it is the common geometry, and $\phi = 180°$ when two bemas are co-propagating.

Before the start of each set of measurements, co- or counter-propagating coupling laser beam is aligned to completely overlap the probe beam through the cell. Then the platform is rotated with interval of $1°$. For each angle, we recorded five traces of the transmission spectra and then averaged them to suppress noise.

3.2   Experimental Transmission Spectra

Fig.3.2 shows the recorded traces of EIT resonances after averaging out the noise with nearly counter- and co-propagating probe and coupling laser beams. Coupling laser detuning is calibrated by the splitting between $45D_{3/2}$ and $45D_{5/2}$ peaks, and zero detuning is set at the top of $45D_{5/2}$ peak. As expected, the counter-propagating laser beams produce the highest and narrowest transmission peak. Compare co-propagating with counter-propagating geometry, transmission peak amplitude re-
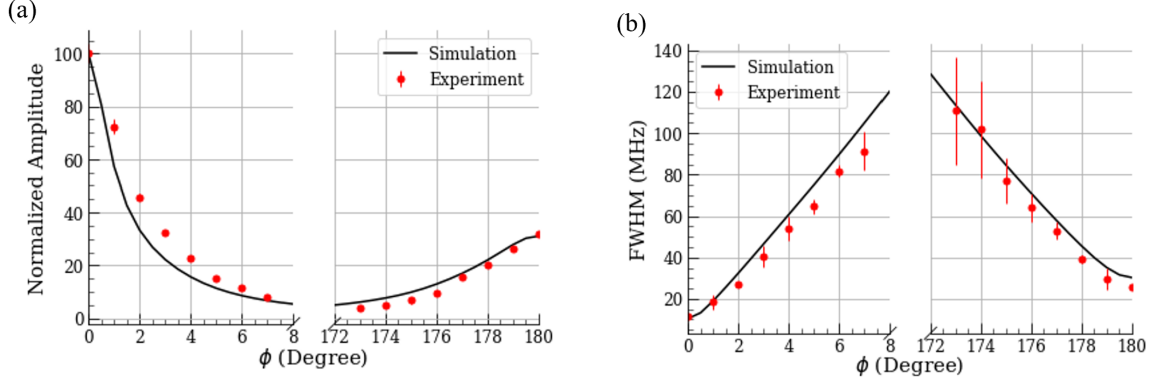
11

(a)

(b)

Figure 3.3: Comparison of amplitude (a) and full width at half maximum (b) of the main EIT resonance (coupling to the $45D_{5/2}$ Rydberg state) between experiment and Rydiqule simulation.

duces to approximately 30%, and width approximately doubles. But in both geometries, we observed strong broadening and amplitude reduction of $45D_{5/2}$ peak even at small angles. In addition, the transmission peak broadens at similar rate in both geometries as crossing angle between two beams increases.

To better compare modification of transmission peak in near co- and counter-propagating geometry, amplitude and full width at half maximum (FWHM) of the $45D_{5/2}$ peak as a function of angle ϕ are plotted in Fig.3.3. Experimental values and error bars on amplitude and FWHM are extracted by conducting a Lorentzian fit of the traces shown in Fig.3.2. Again, all the amplitude is normalized to the value in counter-propagating geometry (the highest $45D_{5/2}$ peak). With the crossing angle as small as 5°, amplitude values drop below 20% of the collinear configurations while the width of the resonance triples.

In addition, we calculate the ratio of relative amplitude over FWHM based on experimental values shown in Fig.3.3. The ratio is an indicator of spectroscopic resolution of EIT resonance. We also calculate the overlap volume of two laser beams relative to collinear geometry as an indicator of spatial resolution. The laser beams
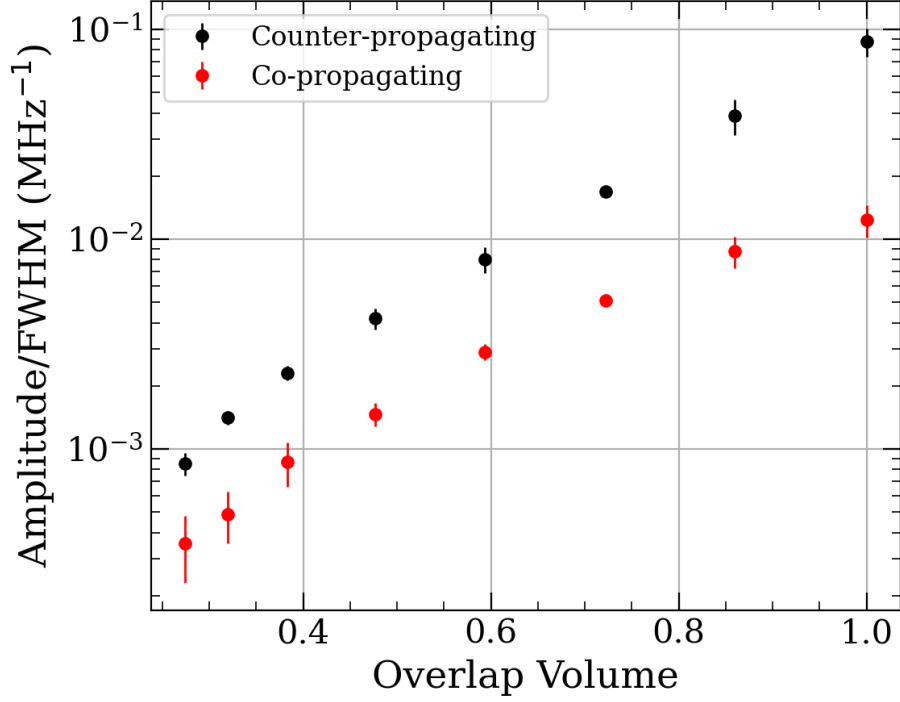
12

Figure 3.4: Trade-off between the spectroscopic and spatial resolution of the crossed-beam EIT resonances. Here we use the experimentally measured ratios between the resonance relative amplitude and width, shown in Fig. 3.3 as a figure of merit for spectroscopic resolution. To characterize the spatial resolution, we use the calculated values of the overlap volume of the two laser beams relative to that in the collinear geometry $\pi d^2 L_{cell}/4 \approx 7$ mm^3.

are modeled as perfect cylinders, and the overlap volume of the two cylinders crossed at angle ϕ is calculated by using the built-in *RegionIntersection* function in Mathematica. The ratio of relative amplitude over FWHM is plotted as a function of overlap volume for both counter- and co-propagation configurations in Fig.3.4 to explicitly show the tradeoff between spatial and spectral resolution of EIT resonances in crossed-beam geometry. The plot shows that counter-propagation geometry is always better than co-propagation for the same spatial resolution.

Results from our experiment indicate that sensitivity of EIT decreases significantly when it is implemented with crossed-beam geometry. And to make localized mea-

surements, it is best to add small angles to counter-propagating beams rather than co-propagating beams. In the following sections, we theoretically discuss the main factor that causes the rapid deterioration of EIT peak in non-collinear geometry and present simulation results that show good agreement with experimental results to verify our theoretical explanation.

3.3 Transverse Velocity Dependence

Consider probe and coupling beam crossing with angle ϕ as in Fig.1.2(b). Based on Eq.2.2, two-photon detuning with velocity dependence $\delta(\vec{v})$ can be rewritten as:

$$\delta(\vec{v}) = \delta_0 - (k_p - k_c \cos\phi)\, v_\parallel + k_c \sin\phi v_\perp \tag{3.1}$$

where δ_0 is the two-photon detuning for stationary atom, $v_\parallel$ is the longitudinal velocity relative to the propagation direction of probe beam, and $v_\perp$ is the velocity component in the transverse direction.

In collinear geometry ($\phi = 0°$ or $180°$), $v_\perp$ term equals zero. Only the longitudinal velocity affects the two-photon detuning in this case, and atoms with different transverse velocity contribute to EIT resonance in the same way. As a result, EIT peak is relatively narrow when we averaged over all transverse velocity groups, as shown in Fig.3.5.

In non-collinear geometry with small crossing angle, $v_\parallel$ term in Eq.3.3 does not change much as $\cos\phi \approx 1$ for small ϕ, and thus dependence on longitudinal velocity is largely the same. However, $v_\perp$ term is non-zero in this case, so EIT resonance now depends on the transverse velocity. Fig.3.5 shows that atoms in different transverse velocity group are on EIT resonance at different coupling detunings. Therefore, the resulting EIT peak for $\phi = 10°$ averaged over transverse velocity distribution is much broader and weaker than the peak with counter-propagating beams.
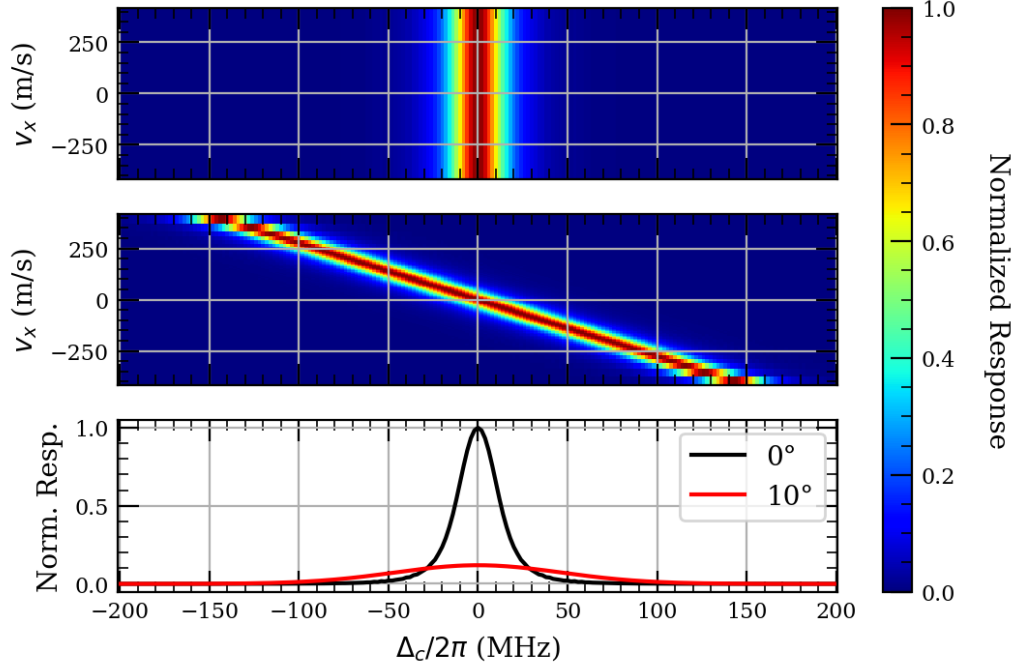
Figure 3.5: Transmission for different transverse velocity groups for (a) counter-propagating geometry and (b) $\phi = 10°$ non-collinear geometry. (c) Comparison of EIT transmission peak averaged over transverse velocity groups in (a) and (b).

3.4 Numerical Modeling

To better understand EIT modification in non-collinear geometry, a numerical model is built. The model includes the four energy levels shown in Fig.3.1(a). Similar to Eq.2.1, Hamiltonian of the system in rotating frame is

$$H = \frac{\hbar}{2} \begin{pmatrix} 0 & \Omega_p^* & 0 & 0 \\ \Omega_p & -2\Delta_p & \Omega_{c,5/2}^* & 0 \\ 0 & \Omega_{c,5/2} & -2\delta & \Omega_{c,3/2}^* \\ 0 & 0 & \Omega_{c,3/2} & -2(\delta + \Delta_{hfs}) \end{pmatrix} \tag{3.2}$$

where $\delta = \Delta_p + \Delta_c$ is two-photon detuning for $45D_{5/2}$ resonance, Δ_{hfs} is the energy splitting between $45D_{3/2}$ and $45D_{3/2}$. Ω_p is Rabi frequency for probe laser coupled to $5S_{1/2} \to 5P_{3/2}$ transition, and $\Omega_{c,5/2}$ and $\Omega_{c,3/2}$ are Rabi frequencies for coupling laser coupled to $5P_{3/2} \to 45D_{5/2}$ and $5P_{3/2} \to 45D_{3/2}$ transitions respectively.

15

Same as our experiments, probe field is set to be on resonance ($\Delta_p = 0$) and the same coupling field scans across Rydberg transitions to $45D_{5/2}$ and $45D_{3/2}$. The values of Rabi frequencies used in the model are first calculated using Alkali-Rydberg Calculator (ARC) and then optimized such that the ratio of amplitudes for $45D_{5/2}$ peak and $45D_{3/2}$ peak, as well as the width of $45D_{5/2}$ peak from simulated spectra match the experimental spectra for the counter-propagating geometry [6]. This is to account for reduction in power as laser beams travel through glass windows of Rb cell. Rabi frequencies are then fixed for all simulated spectra. All other parameters in the model are calculated using ARC based on experimental values.

To incorporate probe and coupling field crossing at an angle in the model, the direction of the probe field wave vector is fixed and the coupling field wave vector is decomposed into a parallel and perpendicular components. Then we use the built-in Doppler averaging tools within Rydiqule to simulate EIT spectra [7].

To account for the reduced overlap volume of two laser beams and thus decreased number of interacting atoms, the atomic density in the model is scaled according to volume. For simplicity, the laser beams are approximated by perfect cylinders with the diameters equal to the full width half maximum of the laser beams, and overlap volume of the two cylinders crossed at angle ϕ is calculated using the built-in *RegionIntersection* function in Mathematica.

Fig.3.3 shows that results from simulation largely agree with our experimental data. Amplitude drops and width broadens rapidly when even a small crossing angle is added to counter- or co-propagating beams. The deviation of simulation from experimental values might be because the model did not account for Gaussian distribution of laser beam intensity when calculating overlap volume of two laser beams.

Chapter 4

Fluorescence Imaging

This chapter presents another method of observing EIT resonances via fluorescence imaging. It is shown to be able to make localized measurement in collinear geometry, and thus avoiding additional Doppler broadening in crossed-beam geometry.

4.1   Fluorescence from decay

The fluorescence we observe in this experiment is the photon emitted by ^{85}Rb atoms when they decay from the excited state $5P_{3/2}$ to the ground state $5S_{1/2}$, as shown in Fig.4.1. The emitted photon has the same wavelength ($\simeq$ 780nm) that matches the splitting between the two states, and the photon is emitted in random direction.

When atoms are only illuminated by the probe laser, they are excited from the ground state to the excited state $5P_{3/2}$. The intensity of fluorescence is the strongest in this case. However, when the coupling laser beam is added to create EIT, the intensity of fluorescence is weaker. This is because when atoms are in EIT dark state, they are in a superposition of the ground state and the Rydberg state, as suggested by Eq.2.1. Ideally, no population is in the excited $5P_{3/2}$ state and in reality, the population just reduced, when atom is in EIT "dark" state. Therefore, less photon with wavelength $\simeq$ 780nm are emitted, reducing the intensity of fluorescence.
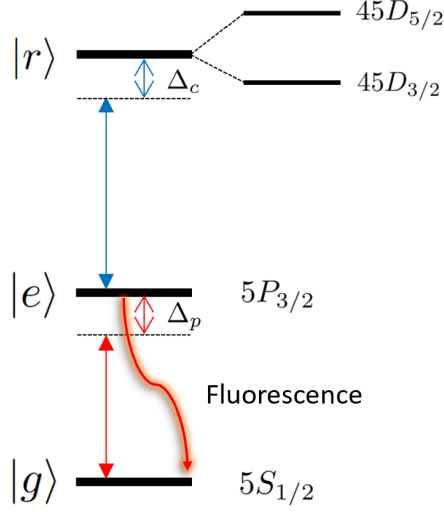
Figure 4.1: Energy level diagram indicating fluorescence.

4.2 Fluorescence imaging method

In the experiment, fluorescence from ^{85}Rb is imaged by a FLIR black-and-white CCD camera placed on the rotational platform such that the camera always faces perpendicular to the propagation direction of the probe beam, as shown in Fig.3.1 and 4.2. A band-pass filter of 780 nm is placed between the cell and camera to filter out light in other wavelengths. Blackout paper is wrapped around the beam path from filter to camera to prevent room light from illuminating the image. A spherical lens is added between the filter and the camera to focus the fluorescence onto the CCD camera. And the position of the lens is fine adjusted to make sure that the camera image can capture the entire length of the cell.

To better compare the fluorescence between EIT and probe-only condition, the probe laser is spatially separated into two beams with approximately equal power by a beam displacer. Both probe beams travel through the cell, but only one beam is overlapped with the blue coupling laser, so only atoms in the channel with both probe and coupling beam will experience EIT. The channel with only the probe
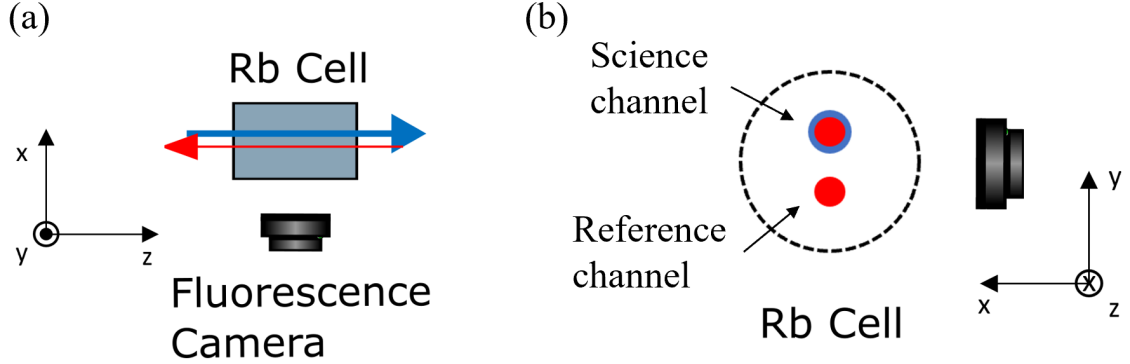
Figure 4.2: (a) Top-down view of the camera setup for fluorescence imaging. (b) Side view of the cell and camera setup. Top channel is the science channel with both red probe and blue coupling beam. Bottom channel is reference channel with only red probe beam.

beam is called the reference channel, and the fluorescence of this channel is used as a reference to account for any change in fluorescence due to the frequency drift of the probe laser. The other channel with both probe and coupling beam is called the science channel, and it is used to see the difference in fluorescence between EIT and probe-only condition.

Similar to the transmission spectra experiment, the probe laser is tuned and locked to the bottom of the $5S_{1/2}$ $F = 3 \rightarrow 5P_{3/2}$ F' optical transition. The coupling laser is parked at the $45D_{5/2}$ EIT peak, which maximizes the population of atoms in the EIT dark state.

4.3 Fluorescence imaging in collinear geometry

In this section, we present the fluorescence images when probe and coupling beam are in collinear geometry. The right two images in Fig.4.3 show the raw fluorescence images taken by the camera. The top stripe is the science channel, and the bottom one is reference channel. While intensity of the bottom channel appears stronger on
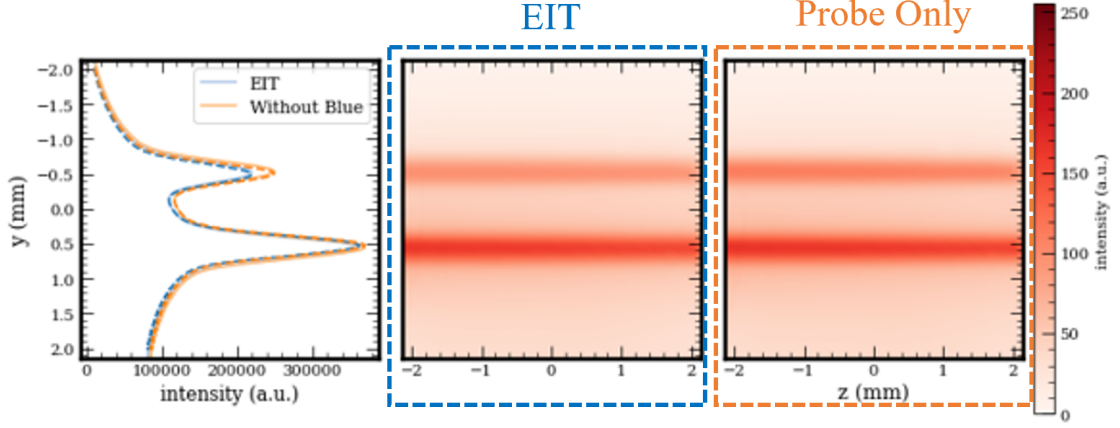
Figure 4.3: The right two images are raw images of fluorescence taken by the camera in counter-propagation geometry. The probe only image is taken when the blue beam is blocked. The EIT image is taken when the blue beam is present in the science channel. Top stripe corresponds to the science channel, and the bottom one corresponds to reference channel. The left plot shows the vertical profile of the two images by integrating each row of the raw image.

the image, the actual intensity of the probe laser beam is the same for both channels. The difference is caused by a constant background with gradient along the vertical axis, which is likely the result of how the imaging system is set up. The background does not affect our experimental results as it is constant among all images, and we focus on the comparison between images rather than between two channels on the same image.

To better compare the difference in fluorescence between probe only and EIT condition, each row of the raw image is integrated to get the vertical profile of the image, as shown in the left plot of Fig.4.3. For the top peak in the plot, which corresponds with the science channel, the amplitude of the peak decreases when atoms are under EIT condition as expected. The fact that the amplitude of lower peak is unchanged between two images indicates the contrast of fluorescence in the science channel is the result of EIT.

20

To quantify the reduction in fluorescence, we fit the vertical profile with two gaussian peaks and background, and we compare the amplitude of the peak for science channel between two images. In counter-propagation geometry, the reduction in fluorescence is around 14% in the science channel. And in co-propagation geometry, the change in fluorescence is weaker, with difference in amplitude being around 4% in the science channel. This agrees with our results in the previous section that show EIT is stronger in the counter-propagation geometry than in co-propagation.

These results confirm that fluorescence imaging with a camera is a practical way to measure EIT resonance with both counter- and co-propagating beams. Although contrast in fluorescence is weaker with co-propagating beams, 4% is enough signal to be used for some measurements, which can be useful in some situation as co-propagation geometry requires simpler setup.

4.4 Fluorescence imaging in a crossed-beam geometry

To capture fluorescence image with crossed probe and coupling beam, we follow similar experimental procedure as measuring transmission spectra. To begin, probe and coupling beam are aligned in collinear geometry. Then, the platform is rotated with interval of $1°$. For every crossing angle ϕ, five images each are taken under EIT and probe-only condition. Multiple images are taken since the contrast in fluorescence to be weaker with crossed beams, and taking average of the images allows us to average out noise in measurement and boost the signal to noise ratio.

We then subtract the averaged image for EIT condition from the image for probe-only condition. The difference in the science channel of two images shows the change in fluorescence induced by EIT.

Fig.4.5 shows the subtracted fluorescence image in near counter-propagation geom-
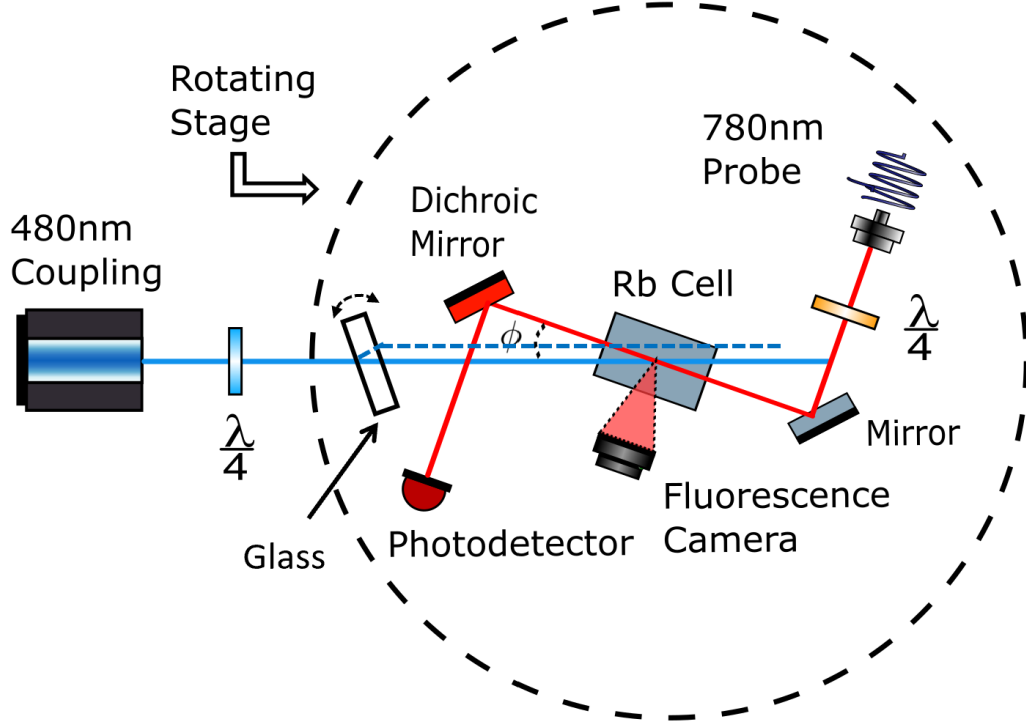
Figure 4.4: Setup schematic with a piece of glass added to shift the crossing point of blue coupling and red probe beam. The piece of glass itself can be rotated independently. All other parts of the setup remain the same.

etry. The red region on the plot corresponds to the region where probe and coupling beam overlap. As expected, the difference in fluorescence is the strongest in collinear configuration ($\phi = 0°$). At $\phi = 2°$, the contrast is lower, but overlap region is not reduced in comparison to $\phi = 0°$. This is because the length of the cell is short so that probe and coupling beam start to overlap outside the cell. At $\phi = 4°$, the contrast weakens further, especially on the two sides, indicating the overlap volume is reduced on two sides. At $\phi = 6°$, the contrast is weak, but the overlap is within the volume of the cell.

These results confirm that EIT resonance is generated locally with crossed-beam geometry. We observe deterioration of EIT resonances via fluorescence imaging as the crossing angle increases. The pattern of deterioration is similar to what we observed
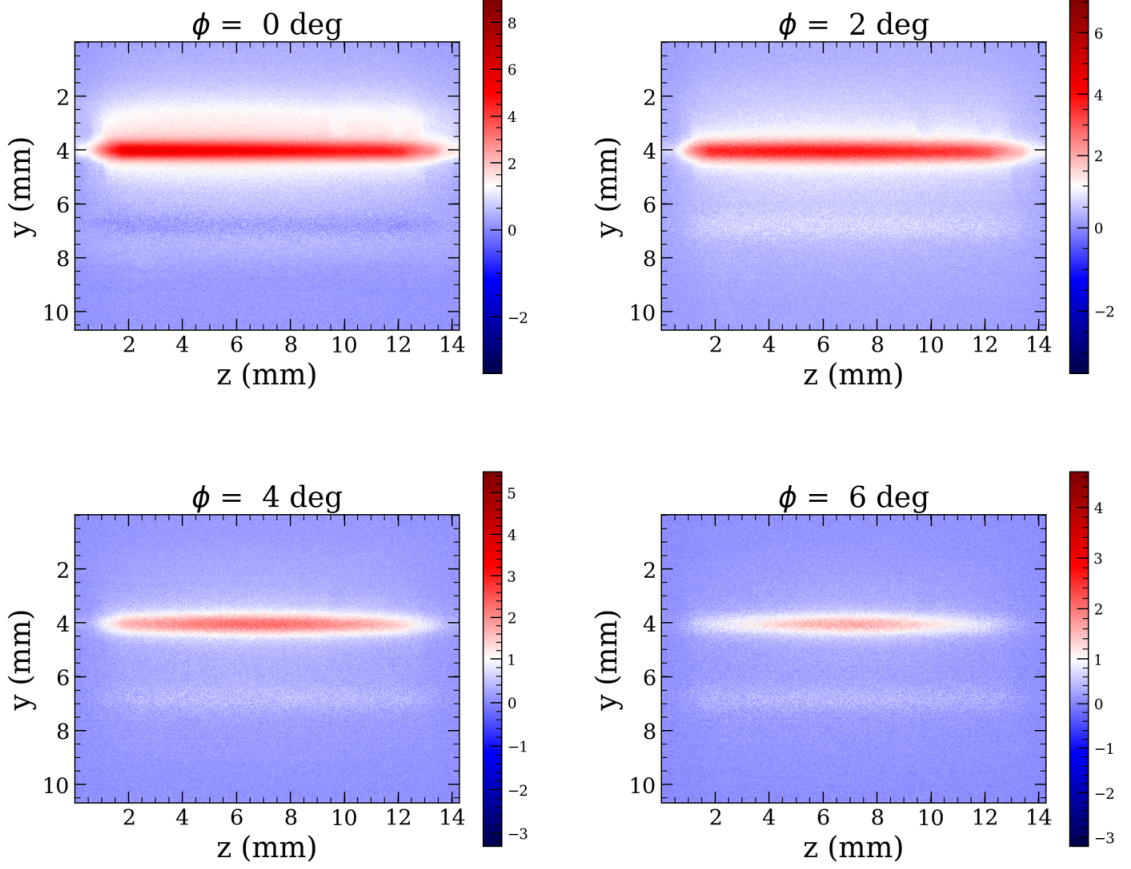
Figure 4.5: Difference between fluorescence images taken with EIT and probe-only condition at various crossing angle ϕ. Note the center of the colorbar is fixed at value of one to boost the contrast shown on the images.

via transmission spectra of the probe beam, which is introduced in previous sections. Moreover, fluorescence imaging also proves that our experimental setup does make the probe and coupling beam to cross near the center of the cell. And as shown in the $\phi = 6°$ image in Fig.4.5, good alignment is maintained as angle ϕ increases. Therefore, we can also confirm that the deterioration of EIT resonances we observed in the previous chapter is not the result of bad alignment.

To test that the red area on the images corresponds to overlap region of probe and coupling beam, we manually change the crossing point of two beams inside the cell

and see if the fluorescence image will change accordingly. The crossing point of two laser beams is controlled by adding a piece of glass in the path of the blue coupling beam, as shown in Fig.4.4. The glass refracts the blue beam a little when tilted at an angle, and the resulting beam path through the cell will be shifted in parallel with respect to beam path without the glass. As a result, the crossing point of two beams will be shifted with the overlap volume being the same.

In order to see the effect of shifting crossing point on fluorescence, we first align the laser beams in collinear geometry with the glass not tilted so that the coupling beam path is unchanged. We then rotate the platform to have two beams crossing at maximum $\phi = 7°$, because the larger the angle ϕ is, the easier to shift the crossing point with tilting the glass.

A set of fluorescence images is first taken with the beam path unchanged, and after subtracting EIT image from probe-only image, we get the difference in fluorescence that should show the crossing point in the middle of the frame. Then the glass is rotated such that the blue beam path is shifted to move the crossing point toward the right on fluorescence image. Then another set of fluorescence images is taken, which should show the crossing point on the right of the frame. Finally, the glass is rotated to the other direction to move the crossing point toward the left on fluorescence images, and resulting graph should have the crossing point appearing on the left of the frame.

Fig.4.6 shows that the change in fluorescence does reflect the spatial shift of laser crossing point. These graphs gives further support that EIT resonances in crossed-beam geometry is local. It also demonstrates a possible way of imaging electric field spatially by crossing two laser beams at multiple points in space.

One advantage of using fluorescence imaging to observe EIT is that it enables spatially resolved measurement with collinear beam. Suppose a beam of electron
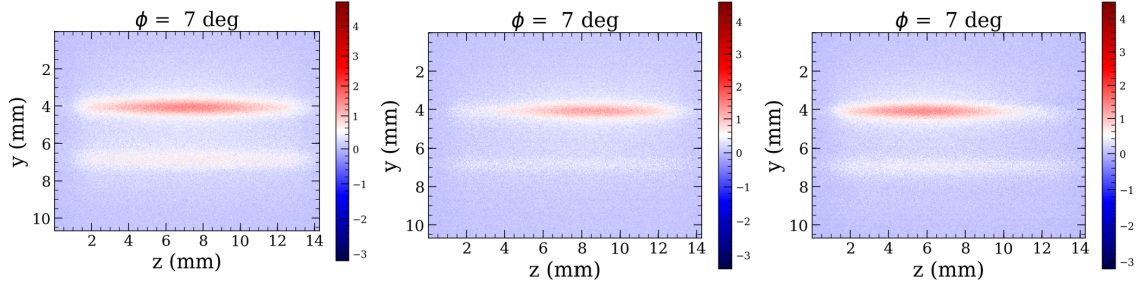
Figure 4.6: Difference between fluorescence images taken with EIT and probe-only condition at crossing angle $\phi = 7°$ with . Note the center of the colorbar is fixed at value of 0.5. It is different from the colorbar in Fig.4.5, so images in two figures are not comparable in terms of color.

goes through the middle of Rb cell along y-direction shown in Fig.4.2. It will induce a local shift of EIT resonance for atoms in the middle of the cell. This change in EIT resonance will affect the fluorescence locally, which can be detected as a change on the fluorescence image shown in Fig.4.3. As a result, the position of the electron beam can be determined based on the fluorescence images without crossing the two laser beams. This indicates fluorescence imaging is capable of measuring spatially non-uniform electric field, while avoiding the additional Doppler broadening discussed in the previous sections. And a collaborative project at NIST demonstrates experimentally that fluorescence imaging can perform two-dimensional imaging of electromagnetic fields [5].

Chapter 5

Toward Doppler-free Measurement with Three-photon EIT

In previous chapters, we have shown that the major limiting factor of two-photon, crossed-beam EIT is the Doppler broadening induced by thermal motion of Rb atoms in the vapor cell. This chapter presents our progress toward implementing EIT in Rb vapor cell with three laser beams, which could enable Doppler-free measurement while providing good spatial resolution. Note that results in this chapter are preliminary as the experiment is developing.

5.1 Three-photon EIT and Doppler-free Geometry

Fig.5.1 shows the energy level diagram of implementing three-photon EIT with ^{85}Rb atoms. Different from two-photon EIT shown in Fig.3.1, atoms are excited from the excited state $|e\rangle$ to the Rydberg state $|r\rangle$ by two laser fields, a dressing laser of 776 nm and a coupling laser of 1258 nm, instead of one coupling laser of 480 nm.

One particular advantage of using three laser fields is the capability of Doppler-free excitation of atoms. In three-photon EIT, the three-photon detuning changes from Eq.2.2 to

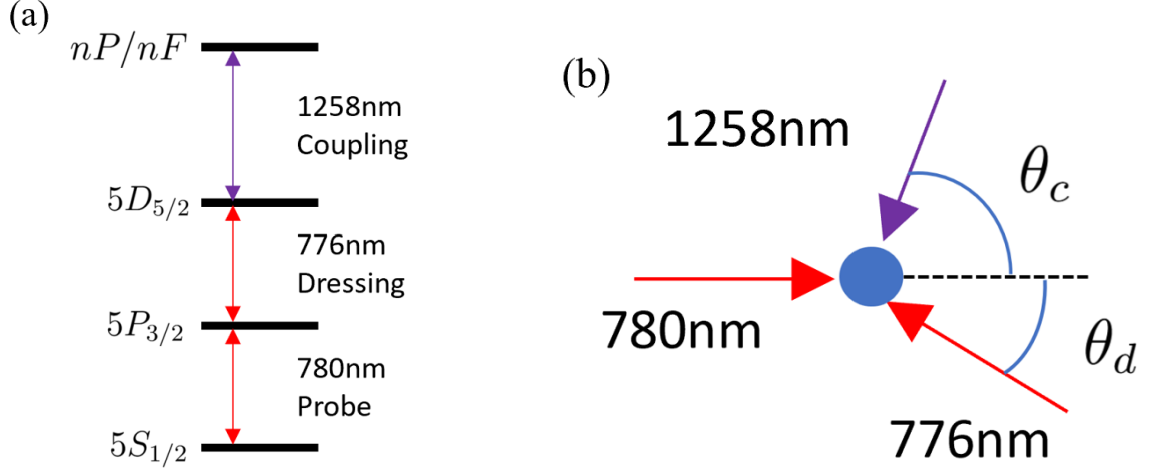$$\delta(\vec{v}) = \delta_0 - (\vec{k}_p + \vec{k}_d + \vec{k}_c) \cdot \vec{v} \tag{5.1}$$

Figure 5.1: (a) Energy level diagram of ^{85}Rb with three-photon EIT. (b) Diagram indicating intersection of three different laser beams.

where $\vec{k}_p$, $\vec{k}_d$, $\vec{k}_c$ are wavevectors of the probe, dressing, and coupling field respectively. Doppler-free excitation requires the condition

$$\vec{k}_p + \vec{k}_d + \vec{k}_c = 0 \tag{5.2}$$

It can be satisfied by crossing the laser beams at specific angles. Using the direction of the probe beam as reference, the dressing beam intersects the probe beam at angle θ_d and the coupling beam intersects at angle θ_c, as shown in Fig.5.1. To satisfy Eq.5.1, we have

$$k_d \ \sin\theta_d = k_c \ \sin\theta_c \tag{5.3}$$

$$k_p = k_d \ \cos\theta_d + k_c \ \cos\theta_c \tag{5.4}$$

Solving two equations by plugging in the wave numbers of three lasers, we get $\theta_d \simeq 36°$ and $\theta_c \simeq 72°$. This confirms that Doppler-free excitation can be achieved with three laser beams, and the fact that three beams cross at non-zero angles with each other allows local measurement to be done with such geometry as well.
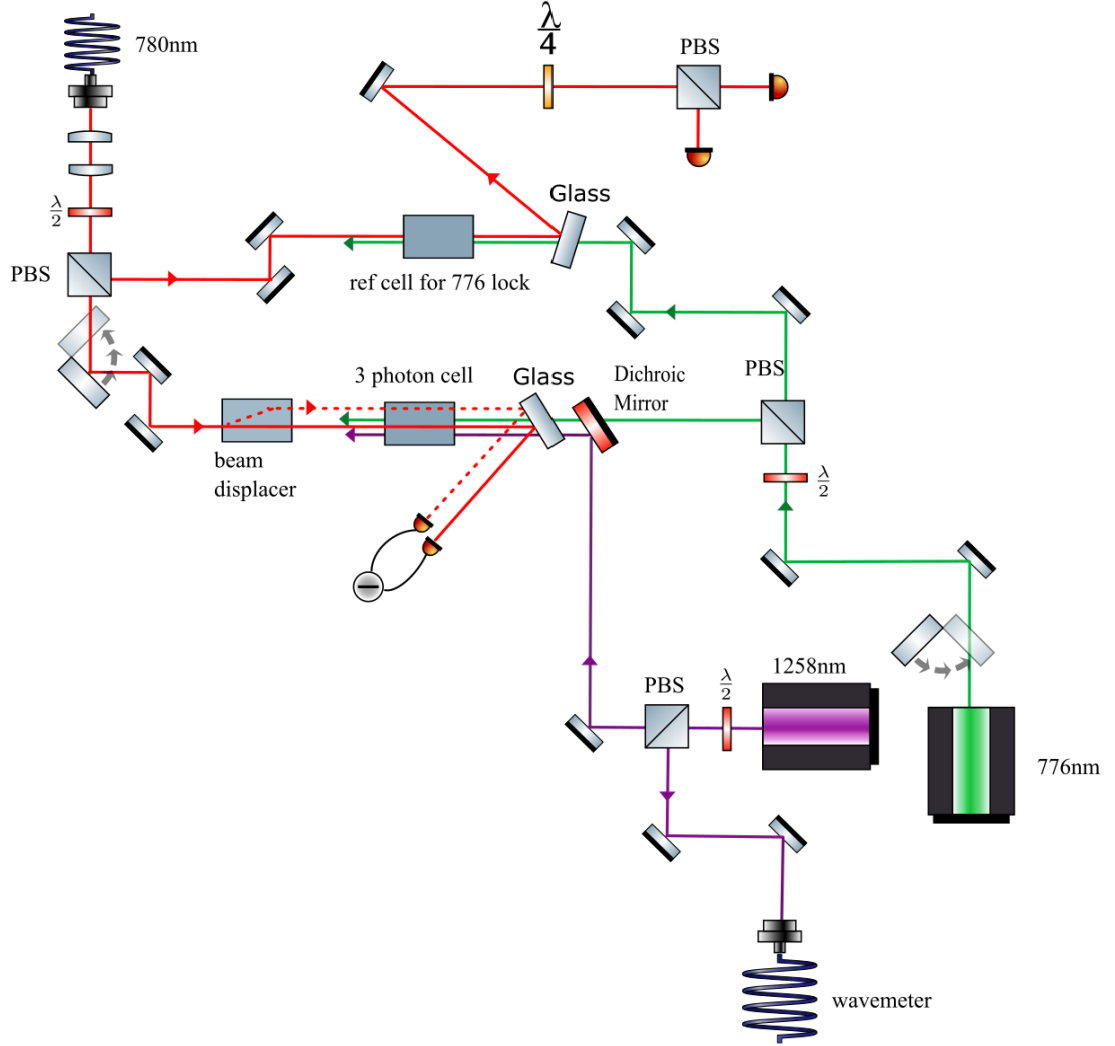
Figure 5.2: Setup schematic for collinear three-photon EIT. $\frac{\lambda}{2}$: half waveplate. $\frac{\lambda}{4}$: quarter waveplate. PBS: Polarized beam splitter.

5.2 Dressing laser stabilization

To implement three-photon EIT, the probe and dressing laser need to be locked to corresponding transitions. The 780nm probe laser is locked to the bottom of the $5S_{1/2}$ $F = 3 \rightarrow 5P_{3/2}$ F' optical transition using saturation spectroscopy. Then two-photon EIT is implemented in another reference cell to lock the 776nm dressing laser, as shown in Fig.5.2. The dressing laser is scanned across the transition to $5D_{5/2}$. The
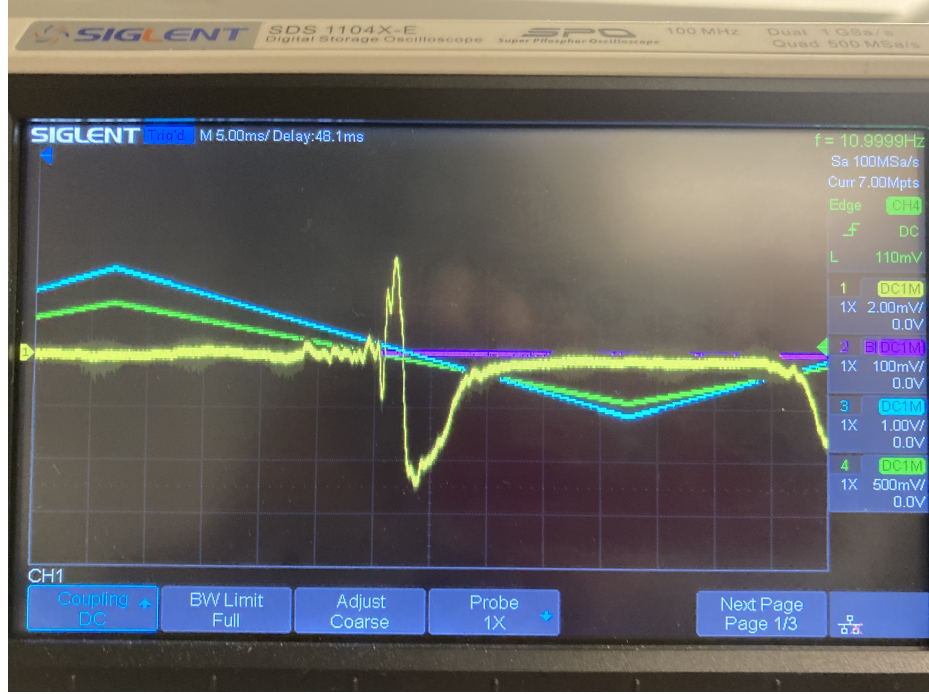
Figure 5.3: Yellow curve is the dispersion signal generated by two-photon EIT in the reference cell.

probe beam is picked up by a piece of glass after going through the cell to observe the EIT resonances. Then a quarter waveplate and a polarized beam splitter separate the probe beam into two beams with opposite circular polarization that are each detected by a channel of a balanced photodetector.

Permanent magnets are placed near two ends of the reference cell to apply an external magnetic field along the cell. The field creates Zeeman splitting of the hyperfine energy levels of ^{85}Rb. As laser light with different polarizations interacts with different hyperfine levels, the Zeeman splitting causes EIT resonances to occur at different frequencies with different dressing beam polarization. Hence, as the dressing laser is scanned across resonance, the two channels of the balanced photodetector will observe EIT resonance at different times. By subtracting signal from two channels, we can get a dispersion signal that is positive when one channel observes EIT res-

onance and negative when the other channel observes the resonance. Fig.5.3 shows the dispersion signal generated in the reference cell. The dispersion creates a steep slope that crosses zero, which can be used to lock the 776 nm dressing laser.

5.3 Preliminary three-photon EIT

Before implementing three-photon EIT in Doppler-free geometry, we first attempt to observe three-photon EIT resonances in collinear configuration. This is because collinear geometry maximizes the overlap volume of laser beams and thus generates the strongest resonances.

Fig.5.2 shows a schematic of the setup for collinear three-photon EIT. Two Rb vapor cells are used in the experiment. One cell is used as reference for frequency stabilization of the 776 nm dressing laser. The other cell is used to implement three-photon EIT.

In the three-photon cell, the probe beam is aligned to counter-propagate the dressing and coupling beam. It is then picked up by a piece of glass after going through the cell to observe the EIT resonances. As an initial step to find the three-photon EIT resonances, we send only one probe beam through the cell rather than two beams. A photo of the actual working setup is shown in Fig.5.4.

To find the three-photon EIT resonance, we park the probe laser on resonance and scan the dressing laser near resonances. The coupling laser is parked near resonance, and then we tune the offset by hand to slowly scan the coupling laser to find the resonances. As shown in Fig.5.5, a weak resonance peak can be observed when the coupling laser is tuned to excite the transition to $53F_{7/2}$ Rydberg state. The signal confirms we are able to excite ^{85}Rb atoms to the Rydberg state via three-photon excitation scheme.

While the signal is weak, the setup will be upgraded to optimize the three-photon
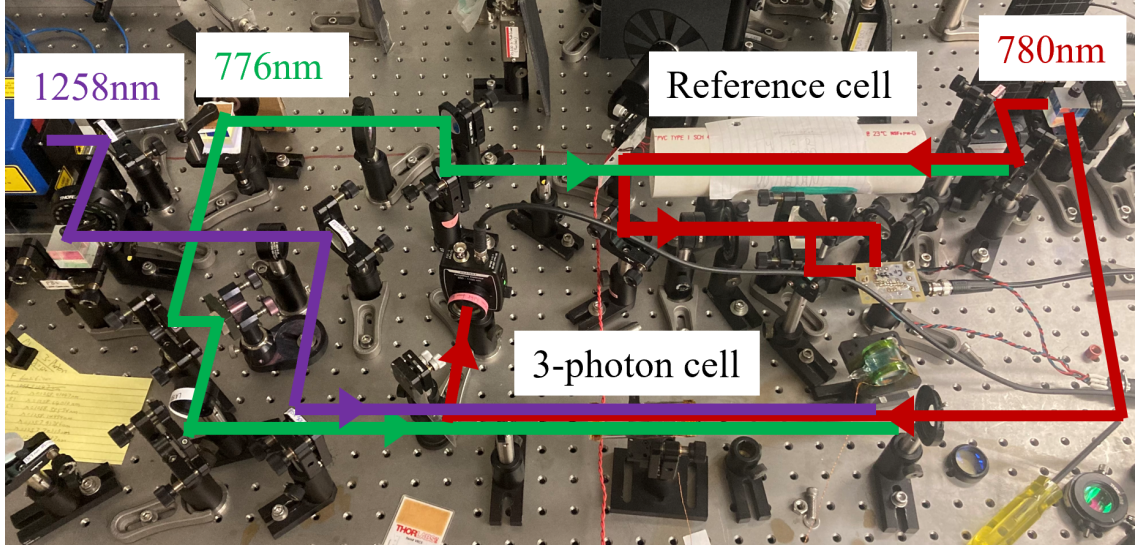
Figure 5.4: Photo of the three-photon setup.

EIT resonances. We are working to collimate and shrink the beam size of the coupling laser to increase its intensity through the cell. Then we plan to observe the three-photon EIT with the probe and dressing laser properly locked. And as we did with two-photon EIT, the power and polarization of three laser beams will be tuned to optimize the resonance. Finally, we could switch to balanced detection as indicated in the design schematic Fig.5.2 to boost the signal.
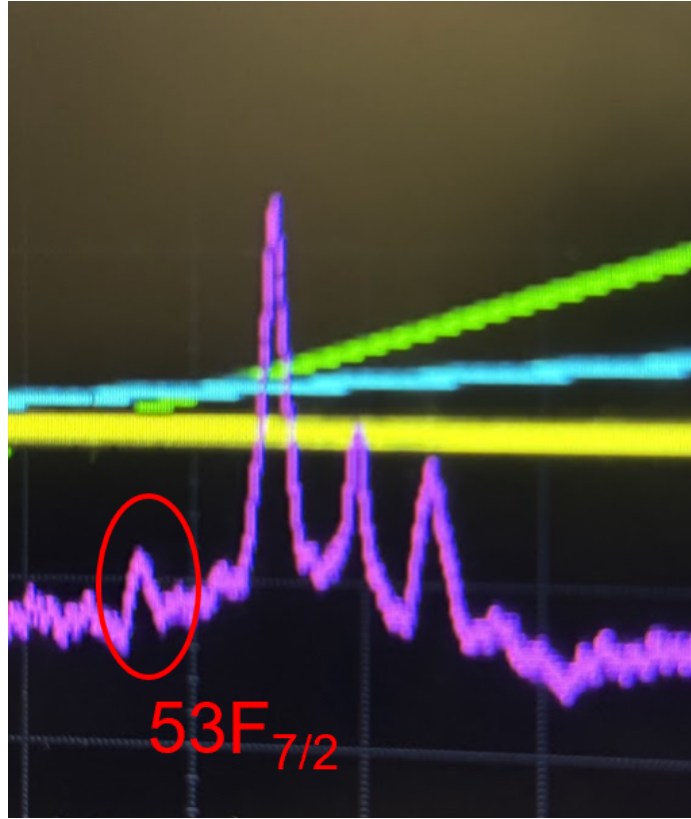
Figure 5.5: Photo of three-photon EIT resonance peak observed on oscilloscope. The peak is observed when coupling laser is tuned near the resonance to $53F_{7/2}$ state. The higher peaks on the side are two-photon EIT resonances created by the probe and dressing laser beam.

Chapter 6

Conclusions and Future Work

In this project, we explore different methods toward making localized measurement of electric field with Rydberg EIT in hot ^{85}Rb vapor. In the first part, we experimentally study the modification of two-photon EIT resonances when two required laser beams are crossed at small non-zero angles. Strong broadening is observed in crossed-beam geometry even crossing angle is small, and tradeoff between spectroscopic and spatial resolution is demonstrated. By numerical modeling, we conclude the deterioration is mainly the result of Doppler effect caused by thermal motion of atoms.

In the second part, we explore fluorescence imaging as an alternative way of observing EIT resonances. Experimental results confirm that signal obtained using this method is strong enough to make measurements, and the intersection region in crossed-beam geometry is indeed local. In addition, our experiment demonstrates that fluorescence imaging is capable of making local measurement in collinear geometry.

We also explored three-photon EIT with three laser beams crossing at specific angles to achieve localized, Doppler-free measurement. As an initial step, we designed and built an experimental setup to implement three-photon EIT in collinear geometry. Our preliminary results show Rydberg resonance is achieved via three-photon excitation scheme. We are in the process of optimizing the signal by upgrading the setup and tuning the power and polarization setting of laser beams. In the future,

modification of three-photon EIT resonances will be studied when it is implemented in crossed-beam geometry.

This project suggests multiple ways of observing EIT resonances locally, yet actual measurement of electric field has not been performed in this project. Another experiment in our research group implements the fluorescence imaging to detect electron beam, and a new setup to explore plasma diagnostic with Rydberg EIT is being built. Studying EIT resonances in these setup with electric field presence will provides more insight into how Rydberg atom based electrometer can be applied to actual measurements.

References

[1]   Lu Ma. "Electromagnetic Field Sensing with Rydberg Atoms in Vapor Cells". Ph.D. thesis. University of Michigan, 2021.

[2]   N. Thaicharoen et al. "Electromagnetically induced transparency, absorption, and microwave-field sensing in a Rb vapor cell with a three-color all-infrared laser system". In: *Phys. Rev. A* 100 (6 Dec. 2019), p. 063427. DOI: 10.1103/PhysRevA.100.063427. URL: https://link.aps.org/doi/10.1103/PhysRevA.100.063427.

[3]   Christopher L. Holloway et al. "Sub-wavelength imaging and field mapping via electromagnetically induced transparency and Autler-Townes splitting in Rydberg atoms". In: *Applied Physics Letters* 104.24 (2014), p. 244102. DOI: 10.1063/1.4883635.

[4]   Ran Finkelstein et al. "A practical guide to electromagnetically induced transparency in atomic vapor". In: *New Journal of Physics* 25.3 (Mar. 2023), p. 035001. DOI: 10.1088/1367-2630/acbc40. URL: https://dx.doi.org/10.1088/1367-2630/acbc40.

[5]   Noah Schlossberger et al. *Two-dimensional imaging of electromagnetic fields via light sheet fluorescence imaging with Rydberg atoms.* 2024. arXiv: 2412.12568 [physics.atom-ph]. URL: https://arxiv.org/abs/2412.12568.

[6]   N. Šibalić et al. "ARC: An open-source library for calculating properties of alkali Rydberg atoms". In: *Computer Physics Communications* 220 (2017), pp. 319–331. ISSN: 0010-4655. DOI: https://doi.org/10.1016/j.cpc.2017.06.015. URL: https://www.sciencedirect.com/science/article/pii/S0010465517301972.

[7]   B. N. Miller et al. "RydIQule: A Graph-based paradigm for modeling Rydberg and atomic sensors". In: *Computer Physics Communications* 294 (2024), p. 108952. DOI: 10.1016/j.cpc.2023.108952. eprint: https://doi.org/10.1016/j.cpc.2023.108952. URL: https://doi.org/10.1016/j.cpc.2023.108952.